High Power Laser Science and Engineering, (2024), Vol. 12, e78, 10 pages.
doi:10.1017/hpl.2024.53

HIGH POWER LASER SCIENCE AND ENGINEERING

RESEARCH ARTICLE

Development of a multifunctional optical diagnostic system at the Shenguang-II upgrade laser facility

Xinyan Li[1], Peng Yuan[1,6], Fan Gao[1], Yifan Liu[1], Lixuan Wu[1], Xiaohui Yuan[2,5], Zhe Zhang[3,4,5], Jie Zhang[2,3,5], Jun Li[1], and Jian Zheng[1,5]

[1]*Department of Plasma Physics and Fusion Engineering, University of Science and Technology of China, Hefei, China*

[2]*Key Laboratory for Laser Plasmas (MoE) and School of Physics and Astronomy, Shanghai Jiao Tong University, Shanghai, China*

[3]*Beijing National Laboratory for Condensed Matter Physics, Institute of Physics, Chinese Academy of Sciences, Beijing, China*

[4]*Songshan Lake Materials Laboratory, Dongguan, China*

[5]*Collaborative Innovation Center of IFSA (CICIFSA), Shanghai Jiao Tong University, Shanghai, China*

[6]*Present address: Tsung-Dao Lee Institute, Shanghai Jiao Tong University, Shanghai, China*

(Received 7 June 2024; revised 12 July 2024; accepted 25 July 2024)

Abstract

A multifunctional optical diagnostic system, which includes an interferometer, a refractometer and a multi-frame shadowgraph, has been developed at the Shenguang-II upgrade laser facility to characterize underdense plasmas in experiments of the double-cone ignition scheme of inertial confinement fusion. The system employs a 266 nm laser as the probe to minimize the refraction effect and allows for flexible switching among three modes of the interferometer, refractometer and multi-frame shadowgraph. The multifunctional module comprises a pair of beam splitters that attenuate the laser, shield stray light and configure the multi-frame and interferometric modules. By adjusting the distance and angle between the beam splitters, the system can be easily adjusted and switched between the modes. Diagnostic results demonstrate that the interferometer can reconstruct electron density below 10^{19} cm^{-3}, while the refractometer can diagnose density approximately up to 10^{20} cm^{-3}. The multi-frame shadowgraph is used to qualitatively characterize the temporal evolution of plasmas in the cases in which the interferometer and refractometer become ineffective.

Keywords: interferometer; multi-frame shadowgraph; optical diagnostic system; refractometer

1. Introduction

Laser-produced plasmas cover a vast parameter space and have significant applications in various fields, such as astrophysics[1], geology[2], agriculture[3], lithography[4] and inertial confinement fusion[5]. In the double-cone ignition (DCI) scheme[6], as well as other laser fusion schemes, such as indirect-drive[5] and hybrid-drive[7], the efficiency of energy coupling between the laser beams and the target is greatly impacted by laser–plasma instabilities (LPIs), which are of great concern in every scheme[8,9]. The sensitive dependence of the LPI level on plasma conditions requires the accurate characterization of plasmas[9], while the transient and inhomogeneous nature of underdense plasmas underscores the importance of acquiring highly spatial- and temporal-resolved data to gain insight into its properties.

Many optical diagnostic techniques have been developed to achieve a comprehensive understanding of laser-produced underdense plasmas[10]. Typically, the laser beam is utilized as a probe to propagate through the plasma to be diagnosed. The parameters of the plasma are then inferred by measuring the phase change (holography/interferometry[11,12]), refraction angle (angular filter refractometer[13,14], schlieren[15,16], grid image refractometry[17]) and displacement (shadowgraphy[15]) of the probe. Each of these diagnostic techniques has a specific range of applicability. For example, shadowgraphy is sensitive to the second derivative of the refractive index and is commonly applied for diagnosing shock waves or plasmas with large density gradients. On the other hand, schlieren surpasses shadowgraphy in detecting weaker perturbations by virtue

Correspondence to: J. Zheng, Department of Plasma Physics and Fusion Engineering, University of Science and Technology of China, Hefei 230026, China. Email: jzheng@ustc.edu.cn

of its sensitivity to the first derivative of the refractive index. Both methods can provide a qualitative image of plasma. However, quantitatively acquiring electron density information presents certain challenges for shadowgraphy and schlieren techniques[10]. Interferometry is an accurate method for measuring electron density and is widely used in plasma diagnostics[18,19]. Although interference fringes indeed exhibit great sensitivity for low-density plasmas, interferometry confronts the difficulty posed by large-integrated phase variation and unresolvable fringes for large-scale and deep-gradient high-density plasmas[13]. In contrast, angular filter refractometry (AFR) is an effective solution to large-scale and deep-gradient high-density plasmas, capable of measuring electron densities up to 10^{21} cm^{-3} with large aperture collection lenses[13], but it becomes insensitive for low-density plasmas[20]. To comprehensively characterize laser-produced plasma, a single diagnostic technique usually is not adequate, so employing multiple diagnostic methods becomes essential. For example, the optical diagnostic systems designed for the OMEGA facility[17] and the Shenguang-II facility[21,22] illustrate the diverse approaches necessary in prevalent plasma diagnostic systems.

The selection of diagnostic methods for plasma is guided by the specific characteristics of each method: interferometry is typically chosen for areas with minimal electron density gradients, refractive angle measurement method is preferred for regions with high-density gradients and shadowgraphy is utilized for the qualitative characterization of areas with even higher density gradients. In the case that our understanding of the target plasma state is insufficient, employing multiple methods to diagnose plasma parameters becomes particularly desired, especially for novel fusion schemes such as DCI. The above-mentioned diagnostics can of course be established independently and separately; however, it is a great advantage to implement a system that can realize easy switching among diagnostic modes in the integrated experiment of laser fusion. In this paper, we report the development of a multifunctional optical diagnostic system, which can be easily switched among the working modes of the interferometer, AFR and multi-frame shadowgraph. The interferometer uniquely separates magnification, fringe spacing and the field of view (FOV). Once the magnification is established, both the fringe spacing and FOV can be independently adjusted in straightforward ways. The AFR employs a strip Fourier filter, different from the traditionally used bulls-eye shape filter[13,20]. This modification facilitates easier phase reconstruction and enables a higher diagnostic limit of electron density achievable with the interferometer. The shadowgraph is realized with an innovative multi-frame photography method that is both compact and versatile, offering straightforward adjustments for the number and temporal delay of frames[23]. The three modes share the most part of the optical system, and are easily switched by inserting corresponding modules. The system is successfully applied to the DCI experiments[24] performed at the Shenguang-II upgrade (SG-II UP) facility.

2. System design

The primary aspect of designing a multifunctional system is to maximize the shared optical components, thereby minimizing the necessary adjustments when switching between diagnostic modes. However, different diagnostic methods require the use of various techniques to 'decode' the probes carrying plasma information, thereby enabling the retrieval of data such as the electron density. For interferometry, generating two coherent beams at the recorder surface is essential, with one beam encoding information about the plasma. The two coherent beams can be spatially separated beams or two regions of the same beam. Typical methods involve optical elements, such as Wollaston prisms or bi-prisms, or beam splitters for a Mach–Zehnder optical path configuration. In AFR, a selective mask is generally necessary only at the Fourier plane. For shadowgraphy, simply imaging the plasma onto the recorder surface suffices. A novel approach is proposed to combine shadow technology with multi-frame photography, facilitating flexible multi-frame imaging of the plasma[23].

A pair of beam splitters is suitable to accommodate the above-mentioned diagnostic configurations. The probe beam is manipulated with the beam splitters, between which there would be a small angle. After multiple transmitting and reflecting cycles, a series of laser pulses separated in direction and time delay is generated. By adjusting the angle between the beam splitters, the spatially separated beams can be controlled to either interfere or not interfere and multi-frame photography can be achieved by recording the time delayed pulses with a gated optical intensifier (GOI)[23]. We maximize the utility of the beam splitters by employing them as an interferometric module, attenuator and multi-frame module in various diagnostic setups, thereby minimizing the adjustments required when switching between diagnostic modes (see Figure 1).

It is desired that the beam intensities on the recorder are roughly the same. The splitting ratio of the beam splitter, that is, the transmission-to-reflection ratio, is an important parameter, as it determines the relative intensities of the generated beams. A splitting ratio of 1:9 is proved suitable for the experiment. Moreover, in order to diagnose laser-produced plasma with a density as high as possible, a 266 nm wavelength laser pulse, with an output energy of approximately 10 mJ and a pulse width of 6.5 ns (full width at half-maximum (FWHM)), is used as the probe. A GOI with a minimum gating time of 200 ps is adopted for time-gated recording. A schematic diagram of the system is illustrated in Figure 1. After passing through plasma, the probe is collected and aligned with a pair of 2-inch confocal

https://doi.org/10.1017/hpl.2024.53 Published online by Cambridge University Press

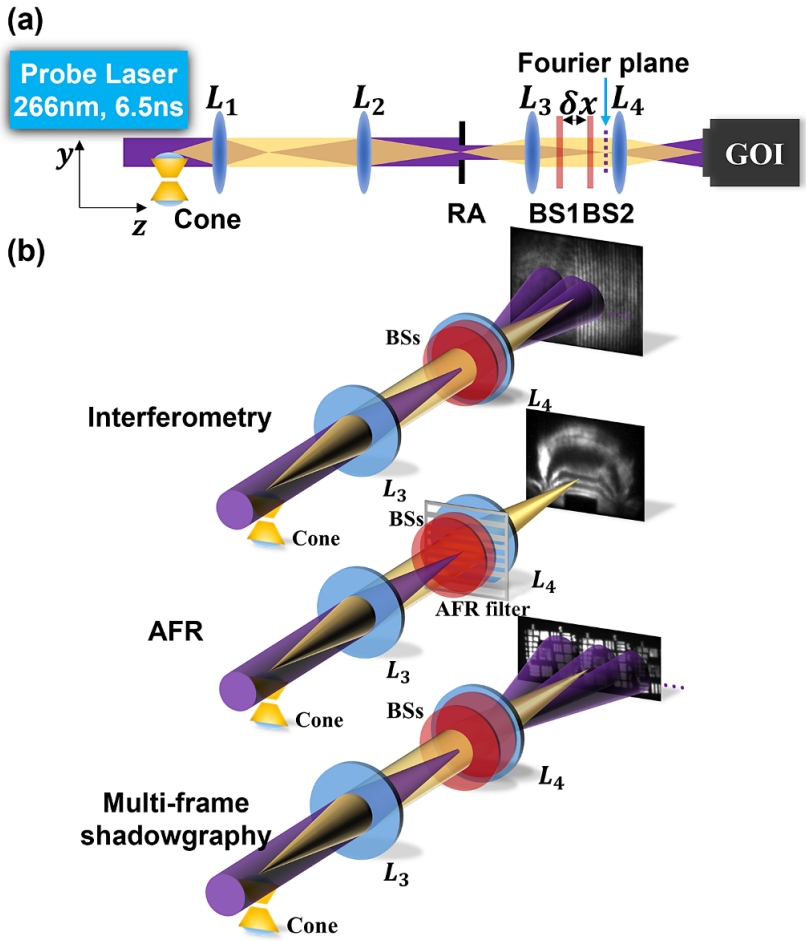

Figure 1. (a) Schematic of the entire system. The focal lengths of lenses L_1, L_2, L_3 and L_4 are 40, 80, 60 and 80 cm, respectively. (b) Optical arrangement schematic for various diagnostics modes. A rectangular aperture (RA) is used to limit the FOV of the relay image on the GOI, preventing crosstalk between the images. The distance δx between beam splitters plays a crucial role in the multi-frame shadowgraph mode, as it determines the framing time interval. In the interferometer mode, this distance is set to be sufficiently small. In the AFR mode, a streak filter is positioned at the Fourier plane, and the beam splitters merely serve to attenuate the probe and shield against stray light.

lenses L_1 and L_2, and the size of the image is limited by a rectangular aperture (RA) and then relayed to the GOI with another pair of 2-inch lenses L_3 and L_4. The initial imaging part, composed of the first pair of lenses L_1 and L_2, relays the plasma image from the target chamber center (TCC) to an RA. When switching between different diagnostic modes, it is only necessary to adjust the module located between lenses L_3 and L_4, as illustrated in Figure 1. The imaging result of a United States Air Force (USAF) test target indicates a magnification of 2.4 in our system, as shown in Figure 2. Two beam splitters are integrated into the optical path to fulfill functions such as intensity attenuation, stray light shielding and the assembly of both the multi-frame and interferometric modules. The slight angular deviation and spatial separation between the beam splitters lead to the spatial separation and temporal delay of the transmitted beams. In addition, the coating on the beam splitters is specifically designed for the 266 nm wavelength, resulting in spatial separation between the stray light and probe on the imaging plane. This configuration effectively shields against stray light, which is a necessary feature in complex laser application environments. Another notable characteristic is the non-confocal arrangement of L_3 and L_4, with L_4 positioned at the focal point of L_3 but slightly out of focus, thereby mitigating the risk of damage. Rapid switching between diagnostics can be accomplished by adjusting the beam splitters, which is discussed in detail below.

2.1. Interferometer

The two beam splitters serve as the interferometric module and attenuator in the interferometer, and the distance δx between beam splitters is set to be significantly smaller than 1 mm. This small distance minimizes the temporal delay between the beams. The two beam splitters are slightly non-parallel, with a small angle θ of the order of milliradians between them. After passing through the beam splitters, multiple transmitted beams are generated with a relatively small angular separation. We can record the interference pattern between any two adjacent beams. The spacing of the

https://doi.org/10.1017/hpl.2024.53 Published online by Cambridge University Press

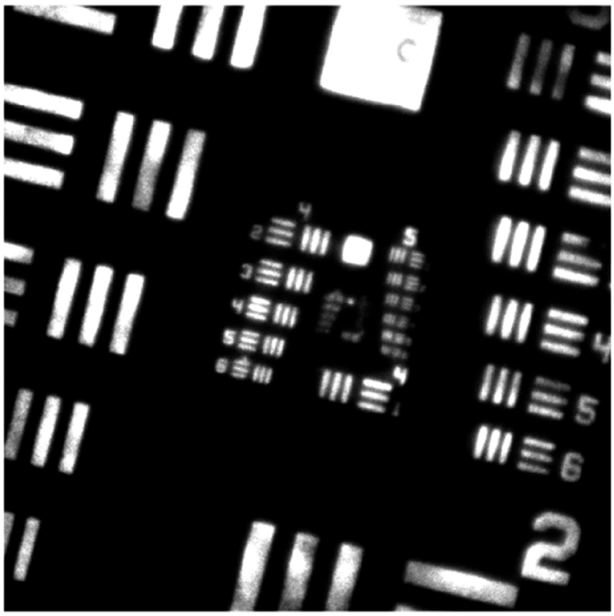

Figure 2. Image of a USAF test target, with an optical system magnification of approximately 2.4 and a contrast value of around 10% for G5E1 (32 lp/mm).

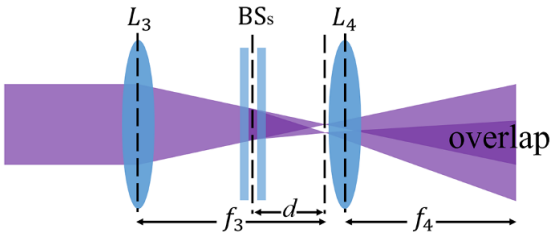

Figure 3. Schematic demonstrating how the beam splitters produce separation and interference. The FOV of the interference is determined by the separation angle of the beam splitters, while the spacing of the fringes is determined by both the separation angle and distance to the Fourier plane.

fringes can be expressed as follows:

$$s = \frac{\lambda f_4}{2\theta d}, \tag{1}$$

where λ is the wavelength of the probe, f_4 is the focal length of L_4 and d is the distance between the center of the two beam splitters and the Fourier plane. The separation distance l between two adjacent beams on the GOI, which represents the width of the interference FOV, can be mathematically expressed as follows:

$$l = 2\theta f_4. \tag{2}$$

The utilization of beam splitters as the interferometric module within the optical system is illustrated in Figure 3, where only two beams are depicted after passing through the beam splitters.

Equations (1) and (2) show the independent adjustment of fringe spacing and the FOV. The former requires manipulation of distance d and angle θ, while the latter only necessitates alteration of angle θ. The two beam splitters are fixed onto a small optical breadboard to facilitate overall movement. Figure 4 shows the interferograms without plasma. Figures 4(a) and 4(b) have different fringe spacing and orientation. The interferograms and reconstructed electron density in the DCI experiments[24,25] are presented in Figure 5. As seen in the figure, the interference fringes are clear and the plasma density can be obtained at a distance from the apex of the golden cone. The fringes become blurred near the apex due to a significant gradient in the plasma density. In order to obtain plasma electron density information near the top of the golden cone, we opt for utilizing the AFR method.

2.2. *Angular filter refractometer*

The AFR method selectively blocks the spatial spectrum of the probe on the Fourier plane and derives the refraction angle of plasma[13]. Instead of using the bulls-eye Fourier filter as previously reported, a streak filter is employed in our experiment. The streak filter only blocks the information in the x direction or y direction on the Fourier plane; the refraction angle Θ_α of the probe beam after passing through the plasma is related to the phase φ of plasma:

$$\Theta_\alpha = \frac{1}{k_0}\frac{\partial \varphi}{\partial \alpha}, \tag{3}$$

where $\alpha = x$ or y, k_0 is the wavenumber of the probe in vacuum and φ is related to the electron density n_e of plasma:

$$\varphi = \frac{k_0}{2}\int_{-\infty}^{\infty}\frac{n_e}{n_c}\mathrm{d}l, \tag{4}$$

where n_c is the critical electron density corresponding to the probe. The outcomes of the placement of the streak filter, featuring straight lines that are parallel to either the x- or y-axis, are illustrated in Figure 6. The streak filter is shown in Figure 7. It facilitates the acquisition of phase results parallel to either the x- or y-axis, in contrast to the bulls-eye filter. Simultaneously, the AFR results can promptly ascertain the symmetry of plasma expansion and rectify it in subsequent shots. Due to the presence of the streak filter, the internal symmetry of the plasma is significantly demonstrated, surpassing that achieved by ordinary schlieren techniques.

A uniform wavefront of the laser probe is crucial for the direct reconstruction of the AFR data, as any nonuniformity in the beam will introduce significant errors during data binarization. While simulation can be utilized for a forward reconstruction of the results, complex cases may require direct phase reconstruction using Equation (3) without simulation. Due to the nonuniformity of the beam profile depicted in the data, significant errors arise during binarization, which subsequently propagate into the reconstruction of electron density. Hence, Figure 8 just displays a preliminary result of

https://doi.org/10.1017/hpl.2024.53 Published online by Cambridge University Press

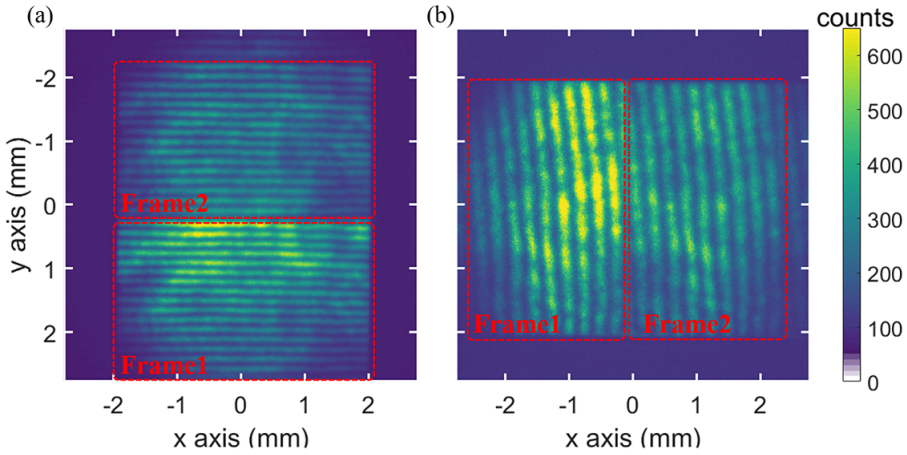

Figure 4. (a) Interferogram without plasma; fringe spacing: 360 μm. (b) Interferogram without plasma; fringe spacing: 640 μm. Frames 1 and 2 in (a) and (b) share the same diagnostic FOV, and they are formed by the interference of the (N−1)th and Nth beams and Nth and (N+1)th beams, respectively.

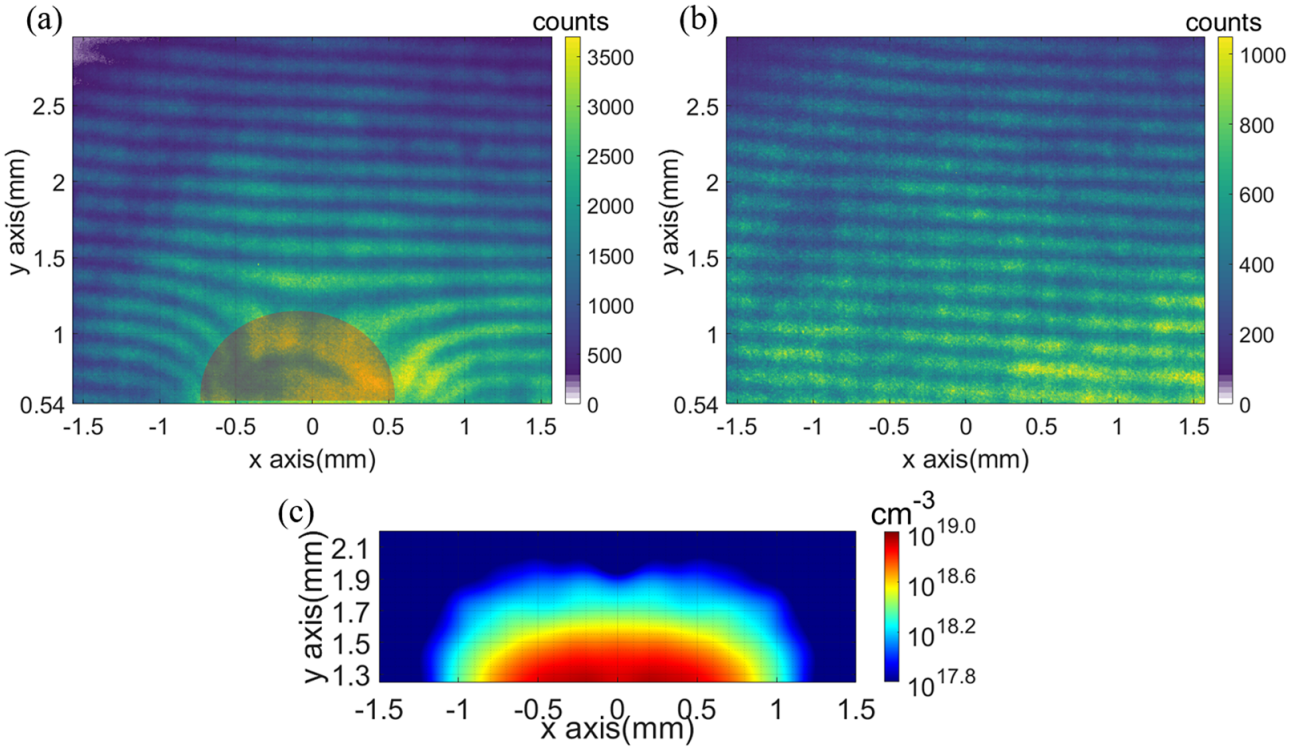

Figure 5. (a) Interferogram with plasma. (b) Interferogram without plasma. (c) Reconstructed electron density. The data in the shaded region in (a) indicate that the fringes are densely packed together due to the large plasma gradient, resulting in being unresolvable. The coordinates of the top of the cone are set as the origin of the coordinates.

the electron density, obtained through the utilization of the reconstruction algorithm explicated in Appendix A.

The preliminary reconstruction results depicted in Figure 8 demonstrate that AFR has obtained electron density data close to 10^{20} cm^{-3}, surpassing the upper limit of interferometer acquisition, as illustrated in Figure 5.

2.3. Multi-frame shadowgraph

The acquisition of plasma evolution information in a single shot is crucial. A novel ultrafast photography technique is employed for plasma diagnosis[23]. In this case, the beam splitters serve as the multi-frame module. Our focus lies on the transmitted beams, which have temporal delay and spatial separation due to the distance δx between the beam splitters and the angle θ. By utilizing the GOI for gated recording, we can obtain the shadowgrams of plasma evolution over time in a single shot. The temporal delay between frames can be adjusted by varying the distance δx between beam splitters, while the number of frames can be controlled by adjusting the angle θ and the size of the RA. A pair of beam splitters can introduce a temporal delay and a unidirectional

https://doi.org/10.1017/hpl.2024.53 Published online by Cambridge University Press

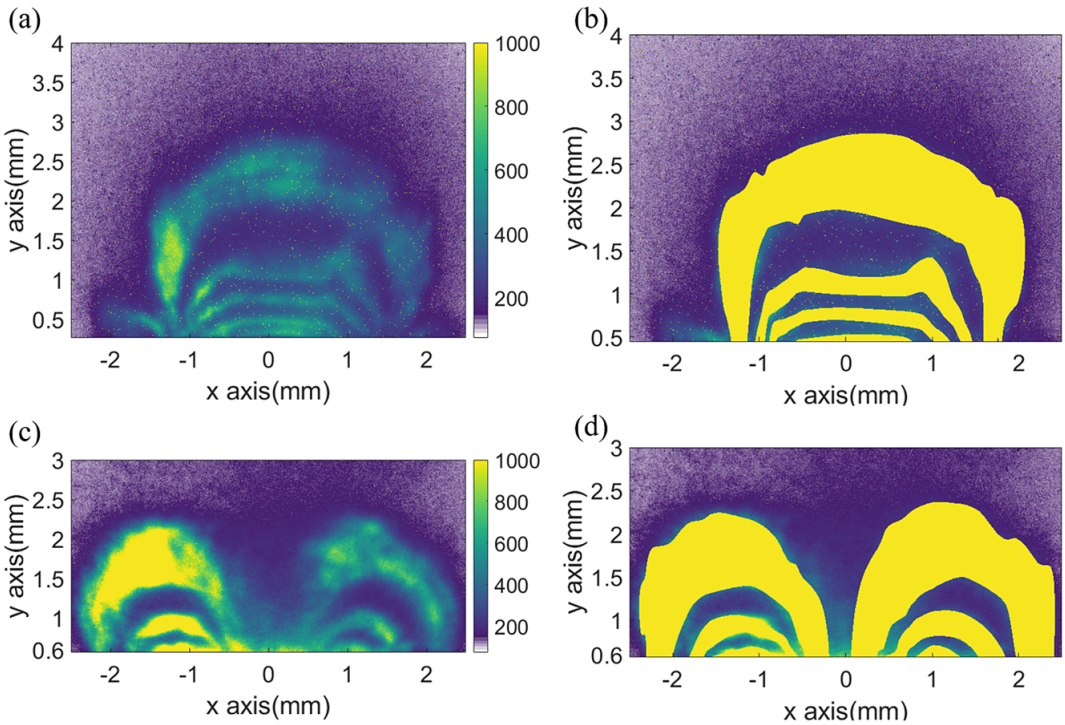

Figure 6. (a) The AFR result with the straight lines parallel to the *x*-axis, and (b) the corresponding preliminary binarization results. (c) The AFR result with the straight lines parallel to the *y*-axis, and (d) the corresponding preliminary binarization results.

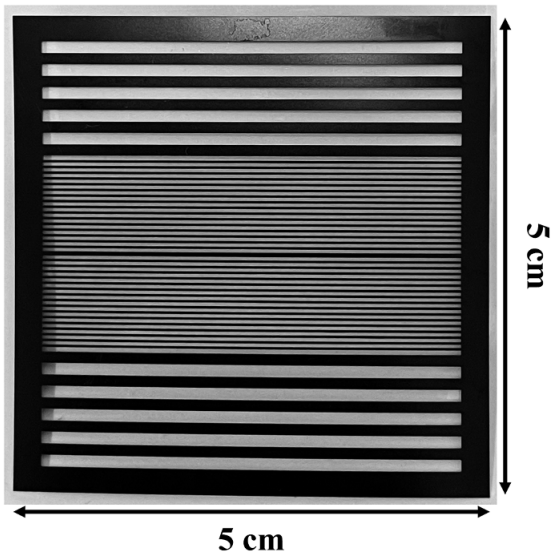

Figure 7. Image of the streak filter.

spatial separation to the transmitted beams. By selecting a suitable distance δx, angle θ and size of the RA, we can acquire multiple shadowgrams with a specific number and temporal delay of frames.

In the DCI scheme, a highly dense plasma is ejected from the tip of the cone[6,26], rendering both the interferometer and AFR ineffective due to the extremely high electron density. The multi-frame shadowgraph is especially well-suited for capturing the temporal evolution of the plasma ejected from the cone. Figure 9 illustrates the pre-shot multi-frame reference shadowgrams, where setting the beam splitter separation to 18 cm results in a time delay of 1.2 ns between frames, and the slight angular deviation between the beam splitters causes the shadowgrams to be arranged horizontally. In frame 1, the position of the cone is annotated, but the tip of the cone is not visible in this data due to the obstruction of the target support structure. Although a pair of beam splitters can be sufficient for recording multi-frame shadowgrams, using two pairs of beam splitters allows the shadowgrams to be arranged along both the *x* and *y* directions, enabling a more comprehensive utilization of the GOI's recording area and finer adjustment of the frame time intervals. To better demonstrate the superiority of multi-frame shadowgraphs in qualitatively recording the temporal evolution of small-scale, ultra-high-density plasmas, we present in Figures 9(b) and 9(c) the dynamic process of the plasma ejected from the tip of the cone captured using two pairs of beam splitters in previous experiments. The difference in intensity between Figures 9(b) and 9(c) is primarily caused by the gating time of the GOI. The near invisibility of frames 1–3 in Figure 9(c) is mainly attributed to the waveform of the laser and the intensity attenuation caused by multiple reflections between the beam splitters. By selecting appropriate beam splitters and adjusting the relative temporal delay between the laser and the GOI, this issue can be significantly alleviated[23]. Figure 10 illustrates the longitudinal scale of the plasma

https://doi.org/10.1017/hpl.2024.53 Published online by Cambridge University Press

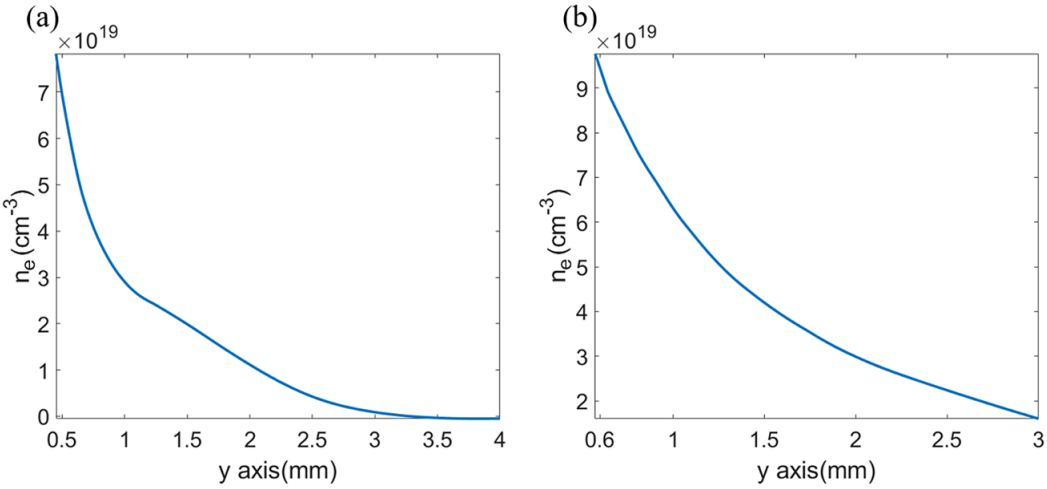

Figure 8. (a) The electron density results at $x = 0$ of Figure 6(a). (b) The electron density results at $x = 0$ of Figure 6(c).

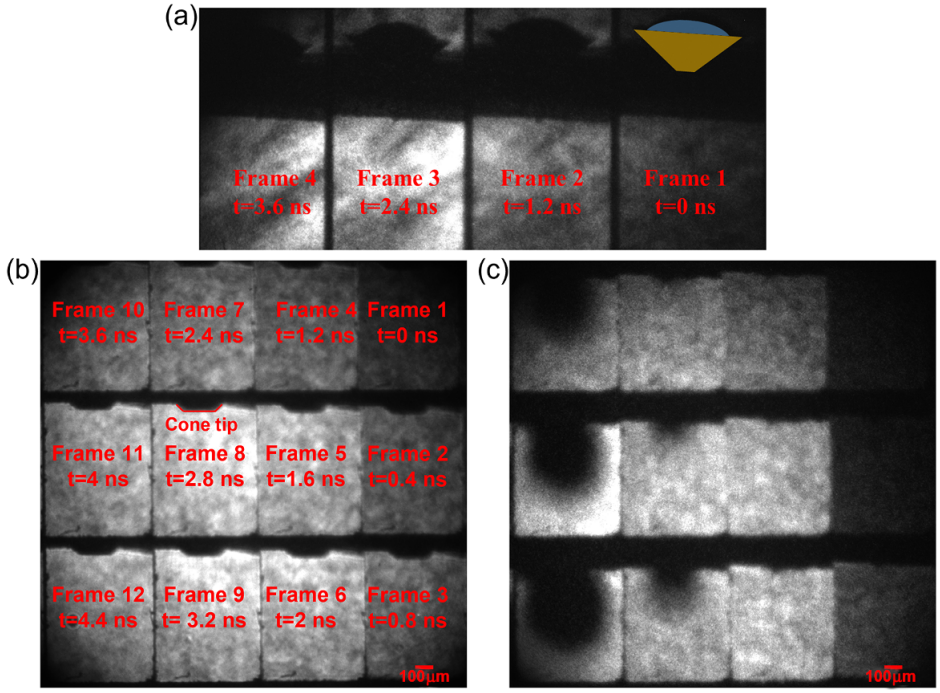

Figure 9. (a) The reference shadowgrams, acquired using one pair of beam splitters, are annotated with the acquisition time for each frame, with frame 1 serving as the temporal baseline. The distance between beam splitters is set to 18 cm, resulting in a time delay of 1.2 ns along the horizontal direction. The obstruction caused by the target holder makes the cone tip invisible, and the estimated position of the cone is indicated in frame 1. (b) The reference shadowgrams, acquired using two pairs of beam splitters, are annotated with the acquisition time for each frame, with frame 1 serving as the temporal baseline. The tip of the cone is denoted in frame 8, with its lateral dimensions measuring approximately 150 μm. The distances between the two pairs of beam splitters are set to 6 and 18 cm, resulting in a time delay of 1.2 ns along the horizontal direction and 0.4 ns along the vertical direction, as illustrated. The gating time of reference shadowgrams is set to 5 ns to observe the field of view of each frame. (c) The plasma shadowgrams corresponding to the reference shadowgrams (b). The gating time of plasma shadowgrams is set to 200 ps to achieve high time resolution of each frame.

ejected from the tip of the cone. The variation in this length is the combined result of the plasma's downward velocity and adiabatic expansion. The lateral scale of the plasma can reflect the results of adiabatic expansion. With the aid of the asymptotic self-similar solution in the point explosion model[27], the internal energy and mass of the fuel can be inferred. Relevant work is currently in preparation.

3. Conclusion

In this paper, we present a multi-functional optical diagnostic system designed for the DCI scheme at the SG-II UP laser facility. This system allows for seamless transitions among the interferometer, refractometer and multi-frame shadowgraph, facilitating comprehensive plasma measurements

https://doi.org/10.1017/hpl.2024.53 Published online by Cambridge University Press

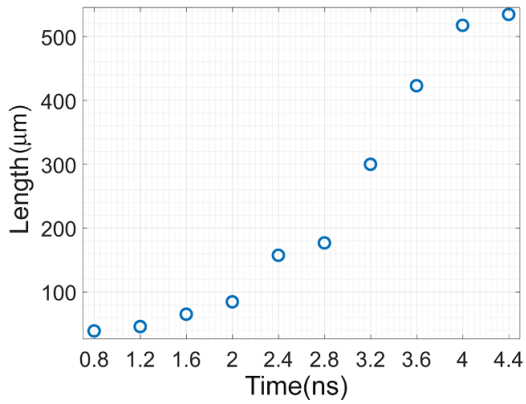

Figure 10. The longitudinal scale of the plasma ejected from the cone tip in Figure 9(c).

across the phase, refraction angle and displacement. The interferometer uniquely separates the control of the fringe arrangement, FOV and system magnification. Once the system is established, it is easy to independently and precisely modify the arrangement of fringes and the FOV. The interferometer effectively diagnoses electron density below 10^{19} cm^{-3}. In regions with a high gradient of electron density, interference fringes become blurred. Instead, AFR is used to diagnose electron densities close to 10^{20} cm^{-3}. For even higher density gradients, where traditional interferometry and AFR fall short, we employ a novel multi-frame shadowgraphy approach. This technique tracks the dynamic changes in high-density plasmas over time, offering unparalleled control over the number and intervals of frames, thus significantly broadening its diagnostic applicability.

Appendix A: Reconstruction method for AFR

Firstly, we need to provide a phase distribution of the plasma and simulate the image of the probe after it passes through the system. Subsequently, data reconstruction is performed. Considering the optical system illustrated in Figure A1, the laser is collected by a 4-f system subsequent to its passage through the plasma and recorded by the GOI. The lens is configured with a focal length of 50 cm, while the probe operates at a wavelength of 266 nm.

The relation between the refraction angle Θ_α of a collimated laser after passing through the plasma and the deflection distance d_α on the Fourier plane can be expressed as follows:

$$d_\alpha = f\Theta_\alpha, \tag{A1}$$

where $\alpha = x$ or y and f is the focal length of the lens as shown in Figure A1. The value of α is dependent on the orientation of the streak filter's straight lines. Specifically, when the streak filter's line is parallel to the x-axis (as depicted in Figure A1), Equations (3) and (A1) yield a value of x for α. We exemplify the reconstruction process with $\alpha = x$, and a similar reconstruction process can be applied to the case where $\alpha = y$.

The plasma phase utilized in the simulation and its corresponding AFR data are depicted in Figure A2, while the streak filter configuration employed in the simulation is presented in Figure A3.

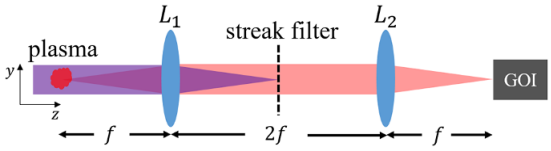

Figure A1. The optical system employed in the simulation.

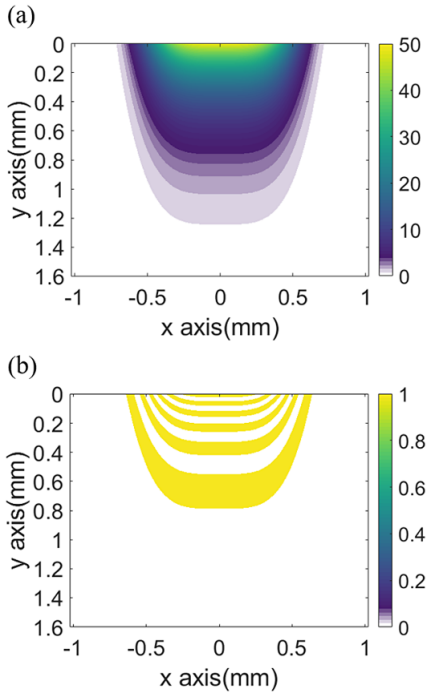

Figure A2. (a) The plasma phase integrated along the z-axis and (b) the corresponding AFR data.

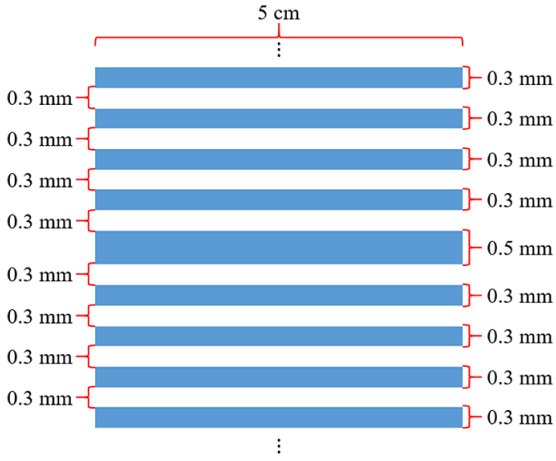

Figure A3. The configuration of the streak filter used in simulation, where the laser is focused at the center of the 0.5 mm wide band.

https://doi.org/10.1017/hpl.2024.53 Published online by Cambridge University Press

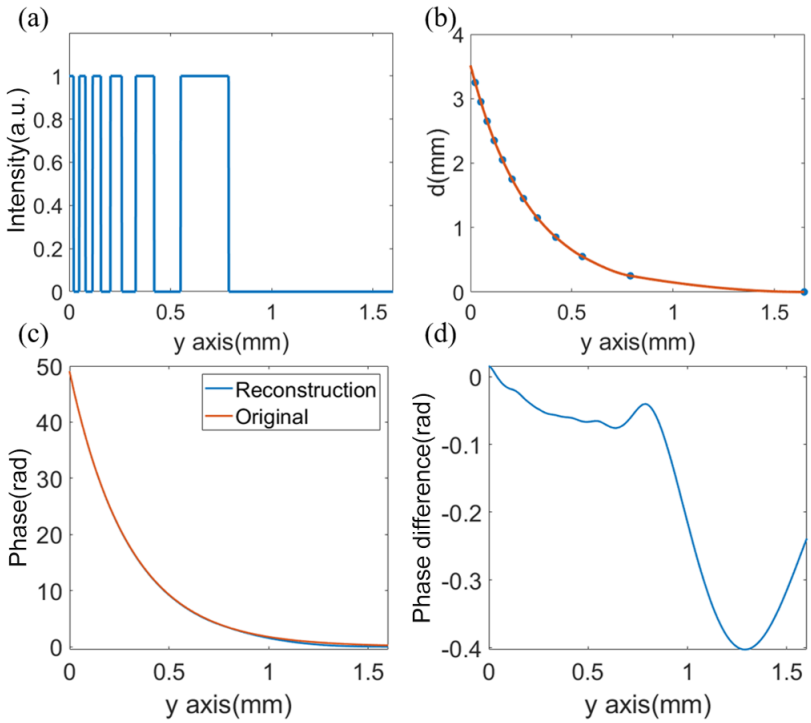

Figure A4. (a) The AFR data at $x = 0$. (b) The deflection distance obtained from Figure A3 and panel (a), where the orange curve represents the fitting of the points, assuming a deflection distance of 0 in the region where plasma diffusion has not yet occurred. (c) The reconstructed phase and the original phase used in simulation. (d) The difference between the reconstructed phase and the original phase.

Reconstruction of the phase at $x = 0$ is demonstrated as an example, where direct processing is applied to the binarized data. Figure A4(a) shows the AFR data at $x = 0$. The edge of each band corresponds to a specific deflection distance of the laser on the Fourier plane, which can be obtained as shown in Figure A4(b). The fitting curve is also presented in this figure. Subsequently, the plasma phase can be obtained based on Equations (3) and (A1). Figure A4(c) illustrates the reconstructed phase and the original phase employed in simulation, while Figure A4(d) presents the corresponding phase error.

Acknowledgements

The authors acknowledge the staff of the DCI team for helping with the experiments. The authors acknowledge Neng Hua, Zhijian Cai, Zhiyong Xie and the staff of the SG-II UP laser facility for operating the laser and target area, and the target fabrication group. This work was supported by the Strategic Priority Research Program of the Chinese Academy of Sciences (No. XDA25010200), the National Key R&D Program of China (No. 2023YFA160005602) and the National Natural Science Foundation of China (No. 12375242).

References

1. W. Yao, A. Fazzini, S. N. Chen, K. Burdonov, P. Antici, J. Béard, S. Bolaños, A. Ciardi, R. Diab, E. D. Filippov, S. Kisyov, V. Lelasseux, M. Miceli, Q. Moreno, V. Nastasa, S. Orlando, S. Pikuz, D. C. Popescu, G. Revet, X. Ribeyre, E. d'Humières, and J. Fuchs, Nat. Phys. **17**, 1177 (2021).
2. C. Fabre, Spectrochim. Acta Part B **166**, 105799 (2020).
3. G. Nicolodelli, J. Cabral, C. R. Menegatti, B. Marangoni, and G. S. Senesi, TrAC Trends Anal. Chem. **115**, 70 (2019).
4. O. O. Versolato, J. Sheil, S. Witte, W. Ubachs, and R. Hoekstra, J. Opt. **24**, 054014 (2022).
5. A. B. Zylstra, O. A. Hurricane, D. A. Callahan, A. L. Kritcher, J. E. Ralph, H. F. Robey, J. S. Ross, C. V. Young, K. L. Baker, D. T. Casey, T. Doppner, L. Divol, M. Hohenberger, S. Le Pape, A. Pak, P. K. Patel, R. Tommasini, S. J. Ali, P. A. Amendt, L. J. Atherton, B. Bachmann, D. Bailey, L. R. Benedetti, L. Berzak Hopkins, R. Betti, S. D. Bhandarkar, J. Biener, R. M. Bionta, N. W. Birge, E. J. Bond, D. K. Bradley, T. Braun, T. M. Briggs, M. W. Bruhn, P. M. Celliers, B. Chang, T. Chapman, H. Chen, C. Choate, A. R. Christopherson, D. S. Clark, J. W. Crippen, E. L. Dewald, T. R. Dittrich, M. J. Edwards, W. A. Farmer, J. E. Field, D. Fittinghoff, J. Frenje, J. Gaffney, M. G. Johnson, S. H. Glenzer, G. P. Grim, S. Haan, K. D. Hahn, G. N. Hall, B. A. Hammel, J. Harte, E. Hartouni, J. E. Heebner, V. J. Hernandez, H. Herrmann, M. C. Herrmann, D. E. Hinkel, D. D. Ho, J. P. Holder, W. W. Hsing, H. Huang, K. D. Humbird, N. Izumi, L. C. Jarrott, J. Jeet, O. Jones, G. D. Kerbel, S. M. Kerr, S. F. Khan, J. Kilkenny, Y. Kim, H. G. Kleinrath, V. G. Kleinrath, C. Kong, J. M. Koning, J. J. Kroll, M. K. G. Kruse, B. Kustowski, O. L. Landen, S. Langer, D. Larson, N. C. Lemos, J. D. Lindl, T. Ma, M. J. MacDonald, B. J. MacGowan, A. J. Mackinnon, S. A. MacLaren, A. G. MacPhee, M. M. Marinak, D. A. Mariscal, E. V. Marley, L. Masse, K. Meaney, N. B. Meezan, P. A. Michel, M. Millot, J. L. Milovich, J. D. Moody, A. S. Moore, J. W. Morton, T. Murphy, K. Newman, J. G. Di Nicola, A. Nikroo, R. Nora, M. V. Patel, L. J. Pelz, J. L. Peterson, Y. Ping, B. B. Pollock, M. Ratledge, N. G. Rice, H.

https://doi.org/10.1017/hpl.2024.53 Published online by Cambridge University Press

Rinderknecht, M. Rosen, M. S. Rubery, J. D. Salmonson, J. Sater, S. Schiaffino, D. J. Schlossberg, M. B. Schneider, C. R. Schroeder, H. A. Scott, S. M. Sepke, K. Sequoia, M. W. Sherlock, S. Shin, V. A. Smalyuk, B. K. Spears, P. T. Springer, M. Stadermann, S. Stoupin, D. J. Strozzi, L. J. Suter, C. A. Thomas, R. P. J. Town, E. R. Tubman, C. Trosseille, P. L. Volegov, C. R. Weber, K. Widmann, C. Wild, C. H. Wilde, B. M. Van Wonterghem, D. T. Woods, B. N. Woodworth, M. Yamaguchi, S. T. Yang, and G. B. Zimmerman, Nature **601**, 542 (2022).
6. J. Zhang, W. M. Wang, X. H. Yang, D. Wu, Y. Y. Ma, J. L. Jiao, Z. Zhang, F. Y. Wu, X. H. Yuan, Y. T. Li, and J. Q. Zhu, Philos. Trans. Roy. Soc. A **378**, 20200015 (2020).
7. X. T. He, J. W. Li, Z. F. Fan, L. F. Wang, J. Liu, K. Lan, J. F. Wu, and W. H. Ye, Phys. Plasmas **23**, 082706 (2016).
8. X. Zhao, X. H. Yuan, J. Zheng, Y. F. Dong, K. Glize, Y. H. Zhang, Z. Zhang, and J. Zhang, Rev. Sci. Instrum. **93**, 053505 (2022).
9. E. M. Campbell, V. N. Goncharov, T. C. Sangster, S. P. Regan, P. B. Radha, R. Betti, J. F. Myatt, D. H. Froula, M. J. Rosenberg, I. V. Igumenshchev, W. Seka, A. A. Solodov, A. V. Maximov, J. A. Marozas, T. J. B. Collins, D. Turnbull, F. J. Marshall, A. Shvydky, J. P. Knauer, R. L. McCrory, A. B. Sefkow, M. Hohenberger, P. A. Michel, T. Chapman, L. Masse, C. Goyon, S. Ross, J. W. Bates, M. Karasik, J. Oh, J. Weaver, A. J. Schmitt, K. Obenschain, S. P. Obenschain, S. Reyes, and B. Van Wonterghem, Matter Radiat. Extremes **2**, 37 (2017).
10. S. S. Harilal, M. C. Phillips, D. H. Froula, K. K. Anoop, R. C. Issac, and F. N. Beg, Rev. Mod. Phys. **94**, 035002 (2022).
11. A. Howard, D. Haberberger, R. Boni, R. Brown, and D. H. Froula, Rev. Sci. Instrum. **89**, 10B107 (2018).
12. X.-Y. Li, P. Yuan, W. Liu, W.-Q. Tan, Y.-Y. Liu, and J. Zheng, Appl. Opt. **62**, 4390 (2023).
13. D. Haberberger, S. Ivancic, S. X. Hu, R. Boni, M. Barczys, R. S. Craxton, and D. H. Froula, Phys. Plasmas **21**, 056304 (2014).
14. P. Angland, D. Haberberger, S. T. Ivancic, and D. H. Froula, Rev. Sci. Instrum. **88**, 103510 (2017).
15. G. Settles, *Schlieren and Shadowgraph Techniques* (Springer, 2001).
16. U. Kogelschatz and W. Schneider, Appl. Opt. **11**, 1822 (1972).
17. D. H. Froula, R. Boni, M. Bedzyk, R. S. Craxton, F. Ehrne, S. Ivancic, R. Jungquist, M. J. Shoup, W. Theobald, D. Weiner, N. L. Kugland, and M. C. Rushford, Rev. Sci. Instrum. **83**, 10E523 (2012).
18. G. Xu, N. Kang, Z. Cui, H. Liu, A. Lei, and S. Zhou, Rev. Sci. Instrum. **94**, 123502 (2023).
19. Q. Liu, M. Ma, X. Zhang, B. Zhao, C. Lv, X. Meng, Z. Wang, C. He, B. Tian, X. Xi, F. Liu, and B. Guo, AIP Adv. **11**, 015145 (2021).
20. D. Haberberger, A. Shvydky, V. N. Goncharov, D. Cao, J. Carroll-Nellenback, S. X. Hu, S. T. Ivancic, V. V. Karaseiv, J. P. Knauer, A. V. Maximov, and D. H. Froula, Phys. Rev. Lett. **123**, 235001 (2019).
21. D. Yuan, Y. Li, T. Tao, H. Wei, J. Zhong, B. Zhu, Y. Li, J. Zhao, F. Li, B. Han, Z. Zhang, G. Liang, F. Wang, G.-y. Hu, J. Zheng, S. Jiang, K. Du, Y. Ding, S. Zhou, and J. Zhang, Astrophys. J. **860**, 146 (2018).
22. Y. Ping, J. Zhong, X. Wang, B. Han, W. Sun, Y. Zhang, D. Yuan, C. Xing, J. Wang, Z. Liu, Z. Zhang, B. Qiao, H. Zhang, Y. Li, J. Zhu, G. Zhao, and J. Zhang, Nat. Phys. **19**, 263 (2023).
23. X.-Y. Li, P. Yuan, L.-X. Wu, F. Gao, and J. Zheng, Rev. Sci. Instrum. **94**, 123510 (2023).
24. Z. Liu, F. Wu, Y. Zhang, X. Yuan, Z. Zhang, X. Xu, Y. Xue, J. Tian, J. Zhong, and J. Zhang, Phys. Plasmas **31**, 042704 (2024).
25. D. Yuan, S. Wang, H. Wei, H. Gu, Y. Dai, J. Zhong, Y. Li, G. Zhao, and J. Zhang, High Power Laser Sci. Eng. **12**, e6 (2023).
26. C. Zhang, Y. Zhang, X. Yuan, Z. Zhang, M. Xu, Y. Dai, Y. Dong, H. Gu, Z. Liu, X. Zhao, Y. Li, Y. Li, J. Zhu, and J. Zhang, Chin. Phys. B **33**, 025201 (2023).
27. L. Sedov, *Similarity and Dimensional Methods in Mechanics* (CRC Press, 1993).

https://doi.org/10.1017/hpl.2024.53 Published online by Cambridge University Press